SUPPLEMENTARY MATERIALS

This document provides additional details and analysis to support the results in the main text. Section I provides a detailed description of our nanoconfined water simulation setup. In Section II, we assess the accuracy of the revPBE0-D3 functional for describing O–H dissociation events. Section III contains a rigorous definition of the proton transfer coordinate ν that we use to quantify proton transfer. Sections IV and V show the pressure dependence of proton transfer in the flat-rhombic and hexatic phases, respectively.

I. COMPUTATIONAL DETAILS

The total potential energy for our simulations is the sum of a water-carbon confining potential and a water-water machine learning interatomic potential (MLIP). The confining walls of our system are uniform planes that are kept at a fixed separation width of 5Å. The water molecules form a monolayer plane between these two walls. The interaction between the water molecules and the graphene sheets is treated as a Morse potential that acts uniformly in the direction perpendicular to the plane of water molecules. Hence, each atom in our system always experiences two Morse potentials – one from each confining wall. The functional form of this potential V_{morse} is:

$$V_{morse} = D_0\left[\left(1 - e^{-a(r-r_e)}\right)^2 - 1\right] \tag{1}$$

In the above, r is the distance of the atom from the wall. The values of the above parameters are taken from a previous study that fit a Morse potential to match water-carbon interaction energies computed at the quantum Monte Carlo level [1]. These values are $D_0 = 5.78 \times 10^{-2}$ eV, $r_e = 3.85$ Å, and $a = 0.92$ Å^{-1}.

For the water-water interactions, we use the same MLIP as in Ref. 2. This MLIP was trained iteratively using an active learning procedure based on committee disagreement [3]. Over successive generations, the training set was expanded to include configurations spanning a broad range of relevant state points and phases, including monolayer, bilayer, and bulk water phases. Full details of the active learning workflow, training procedure, and validation are given in Ref. 2. In this previous work, this MLIP achieved a root-mean-square energy error of 2.4 meV per water molecule and a force error of 75 meV/Å per water molecule. We also performed extensive additional validation, including correlations between force uncertainty estimates and true errors, direct comparisons of MLIP lattice energies with DFT and QMC benchmarks, force RMSEs across the phase diagram, and explicit AIMD simulations of both the hexatic and superionic phases. The training structures generated by these simulations contain only water molecules, as the water-graphene interactions are handled entirely by the implicit Morse potential described above. Accordingly, the MLIP reflects only the water-water interactions in the system.

Our simulation cells contain 144 water molecules, which has previously been shown to be sufficiently large to avoid finite size effects for this system [2, 4]. Furthermore, due to the short-ranged nature of nuclear quantum effects (NQEs), we believe that this choice remains reasonable for the purposes of our analysis. We perform simulations at lateral pressures of 3.0, 4.5, 6.0, 9.0, and 12.0 GPa. For each lateral pressure, we perform simulations at temperatures from 200 K to 600 K at 20 K intervals. Classical simulations are performed with a timestep of 0.5 femtoseconds with an optimal sampling generalized Langevin equation thermostat. These simulations are performed in the NP_{lat}T ensemble, with a modified Martyna-Tuckerman-Tobias-Klein barostat [2]. A constraint on the lattice vector perpendicular to the lateral plane is used to apply the lateral pressure. Dynamical simulations use a time step of 0.5 femtoseconds and a stochastic velocity rescaling thermostat in the NVT ensemble [5]. Positions are sampled every 100 femtoseconds to estimate transport quantities.

Our NPT path-integral simulations use 32 imaginary-time slices with a PILE thermostat [6] and a timestep of 0.5 femtoseconds. When computing dynamical quantities, we instead run simulations in the NVT ensemble using a stochastic velocity rescaling thermostat [5] with a time constant of 100 femtoseconds. For each temperature and lateral pressure, the initial configuration and simulation cell for these dynamical simulations is taken from the NPT simulation run at the same state point. Dynamical quantities such as the ionic conductivity are estimated on these NVT trajectories from simulations that last at least 1 nanosecond. These long trajectory lengths are possible due to the speedup afforded by the path integral coarse graining simulations (PIGS) method [7]. The PIGS simulations

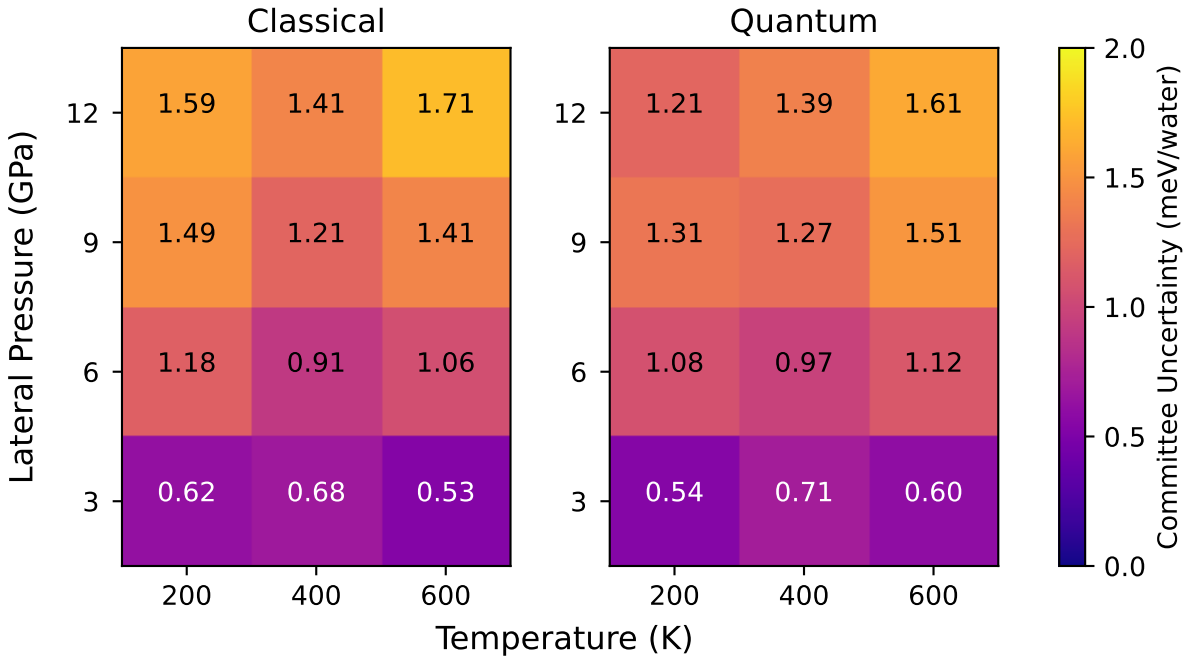

FIG. S1. **MLIP committee uncertainties.** The absolute standard deviations in energy predictions from a committee of eight MLIPs. The individual MLIPs are trained on different subsets of the training set. We refer to trajectories with classical nuclei as "classical", and those from PIMD simulations as "quantum". The conditions shown cover the temperature and pressure conditions considered in this work.

were performed following the protocol illustrated in Ref. 8, wherein the quantum effective potential was estimated from a path integral molecular dynamics simulation at 500 K, within the temperature elevation (Te) approximation. This effective potential was then used to estimate the vibrational spectra of monolayer hexatic water. Since the Te *ansatz* recovers the correct $\omega \to 0$ limit of the vibrational density of states, a single PIGS effective potential can be used to estimate transport quantities across a range of temperatures. Further details on the simulation setup can be found in the input files (to be provided when the manuscript is accepted).

To assess the reliability of the MLIP across both classical and quantum trajectories, we compute the absolute standard deviations in energy predictions from a committee of eight MLIPs trained on different subsets of our training dataset (shown in Fig. S1). These standard deviations serve as a proxy for model uncertainty, which is related to the true error up to a proportionality constant [3]. These uncertainties remain small across all state points, including the highest temperatures and pressure we consider in this work. Notably, the uncertainty values of the quantum (PIMD) trajectories are comparable to those of the classical trajectories at the same state points, indicating that the MLIP maintains accuracy in both regimes. This is likely due to the fact that the high-temperature, high-pressure classical simulations in our training dataset include representative structures from the superionic regime. A more direct analysis of the MLIP's accuracy in describing superionic phases and O–H dissociation events is provided in Section II.

In Fig. 1 of the main text, we provide the phase diagrams of nanoconfined water using both classical and quantum nuclei. To compute these phase diagrams, we estimate the temperature of phase boundaries at each simulated lateral pressure. The boundary between the flat-rhombic and hexatic phases is defined as the temperature at which the flat-rhombic phase ceases to be metastable on the timescale of our simulations, which is approximately 100 picoseconds. Hence, the displayed phase boundary provides an overestimate of the true phase boundary temperature. The hexatic-liquid phase transition has previously been shown to be continuous [2], so we expect the phase transition to be observed nearly instantly, even on our limited simulation timescales. The boundary between the hexatic and superionic phases is chosen as the lowest temperature for which we observe ionic conductivities above 0.1 S/cm. This is the same criterion that we have used for superionic proton transport throughout this manuscript [2, 9]. Finally, the errors in conductivities presented in Fig. V are calculated using the method described in Ref. 10 using the kinisi software [11].

II. BENCHMARKING REVPBE0-D3 FOR BOND BREAKING

To benchmark the performance of the revPBE0-D3 functional (with zero-damping) for bond breaking, we compare its performance to calculations at the level of coupled cluster theory with single, double, and perturbative triple excitations (CCSD(T)) with a local approximation. We start with a snapshot of the monolayer superionic phase from our classical simulations. An example periodic unit cell is shown in Fig. S2. We then select four adjacent water molecules, highlighted in blue, that form a parallelogram-shaped hydrogen bond network. For each selected water molecule, the hydrogen atoms that form the parallelogram are moved incrementally along their hydrogen bond directions in 0.05 Å steps, as indicated by the small arrows in the circled image on the right of Fig. S2. At each increment, the positions of the four water molecules are relaxed using our MLIP, keeping all the other atoms fixed. Single-point calculations are performed along this trajectory at various levels of theory and are summarized in Fig. S3. The density functional theory (DFT) and MLIP calculations are performed on the periodic unit cell, whereas CCSD(T) calculations are performed on a cluster that has been cleaved out from the unit cell, as shown in Fig. S2. In Fig. S3(a), we show that the cluster forward barrier closely matches the periodic unit cell forward barrier within 0.04 kcal/mol.

Overall, we find that the revPBE0-D3 functional agrees with CCSDT(T) on the forward barrier to around 0.5 kcal/mol. On the other hand, the revPBE-D3 functional underestimates the barrier for proton transfer by around 4 kcal/mol. Additionally, the MLIP from Ref. 2 agrees with revPBE0-D3 to around 0.25 kcal/mol, meaning that the MLIP faithfully reproduces the predictions of revPBE0-D3, even during O–H dissociation events. Hence, both the revPBE0-D3 functional and the MLIP agree with CCSD(T) within chemical accuracy.

As described above, the geometry optimization procedure for generating proton transfer trajectories involved optimizing the geometries of four selected water molecules while keeping the remaining water molecules frozen. This approach has two notable consequences. First, because the optimization is performed using the MLIP, the reference CCSD(T) barrier overestimates the true proton transfer energy barrier. Second, the relative stabilities of the two bound states depend on the specific configuration of the background water molecules. For the background configuration used in Fig. S3, geometry optimization yields a lower energy for the second bound state. Repeating

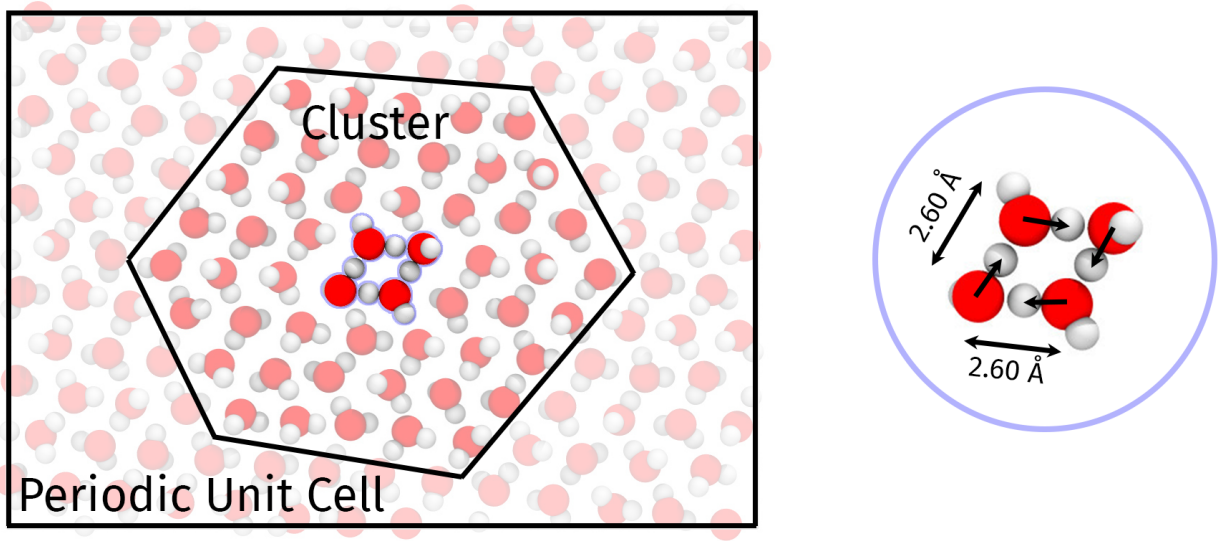

FIG. S2. **The setup used to benchmark DFT functionals.** The left image shows the full periodic unit cell, as well as an example of a cluster of water molecules that are used for our "cluster" calculations. The four central water molecules that are highlighted in blue are shown again in the image on the right. The O–H bond lengths in these highlighted molecules are increased gradually in order to replicate proton transfer. The directions along which the O–H bond length is increased are indicated by the smaller arrows. The parallelogram formed by the four water molecules has an O–O distance of 2.60 Å and a smaller vertex angle of 58.3°.

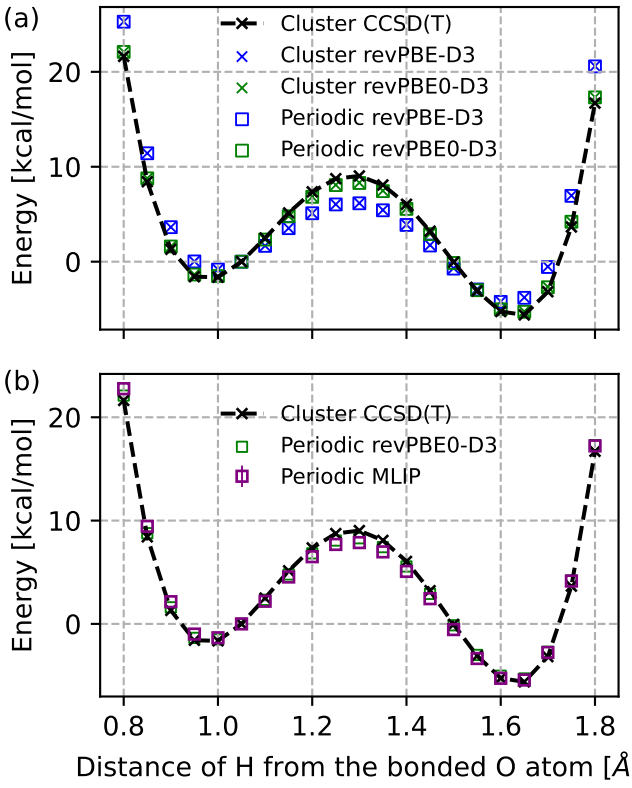

FIG. S3. **Benchmarking density functionals and the MLIP against CCSD(T) for proton transfer.** (a) The energy along the proton hopping barrier in monolayer water estimated at different levels of theory, with both periodic unit cell and cluster calculations. (b) The trained MLIP's proton hopping barrier closely follows that of the underlying revPBE0-D3 functional. Both the MLIP and revPBE0-D3 functional match the forward barrier of CCSD(T) within chemical accuracy. All energies are relative to the bound state with an O–H distance of 1.05 Å.

this procedure with different background configurations would result in varying relative stabilities and energy barriers for the two bound states, which we expect the MLIP to capture accurately based on our benchmarks in this section.

DFT calculations are performed within CP2K [12] while the cluster CCSD(T) calculations are performed with MRCC [13] using the local natural orbital (LNO) approximation to CCSD(T). The CP2K calculations were performed using the Goedecker-Teter-Hutter (GTH) pseudopotentials [14], with the corresponding TZV2P-GTH basis sets. revPBE0-D3 was performed using the auxiliary-density-matrix method [15] for approximating the Fock exchange matrix and energy with the cpFIT3 auxiliary basis set. We perform a two-point extrapolation [16] of the aug-cc-pVTZ and aug-cc-pVQZ Dunning family basis sets [17] with 'normal' LNO thresholds and make a subsequent correction to the 'tight' thresholds performed with the aug-cc-pVTZ basis set.

III. THE PROTON TRANSFER COORDINATE

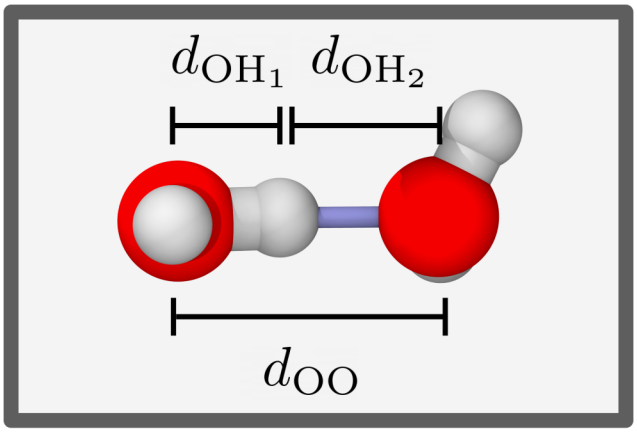

$$\nu = d_{\mathrm{OH}_1} - d_{\mathrm{OH}_2}$$

FIG. S4. **Illustration of the proton transfer coordinate ν.** For a given proton (in white), d_{OH_1} and d_{OH_2} are the scalar distances to the two nearest oxygen atoms (in red). The choice for which oxygen atom corresponds to d_{OH_1} or d_{OH_2} is arbitrary, meaning that the sign of ν is also arbitrary.

In the main text, we use the proton transfer coordinate ν to characterize proton transfer between water molecules. Fig. S4 shows how this coordinate is defined and computed. For each proton, we find the two nearest oxygen atoms. We denote the distance from the proton to each of the oxygen atoms as d_{OH_1} and d_{OH_2}. The proton transfer coordinate ν is then given by the difference of these two scalar distances [18–20]. Since the assignment of d_{OH_1} and d_{OH_2} is arbitrary, the sign of ν is arbitrary, and only the absolute value of ν should be assigned any meaning.

Under this definition, values near $\nu = 0$ correspond to protons that are equidistant from their two neighbouring oxygen atoms, whereas values of ν with large absolute values correspond to protons that are much closer to their nearest oxygen atom than to their second nearest oxygen atom. Importantly, for a proton to transfer from one oxygen to another, it must pass through $\nu = 0$, which allows us to use the free energy barrier along the proton transfer coordinate to understand the kinetics of proton transfer.

IV. PRESSURE-DEPENDENT PROTON DISORDER IN FLAT-RHOMBIC ICE

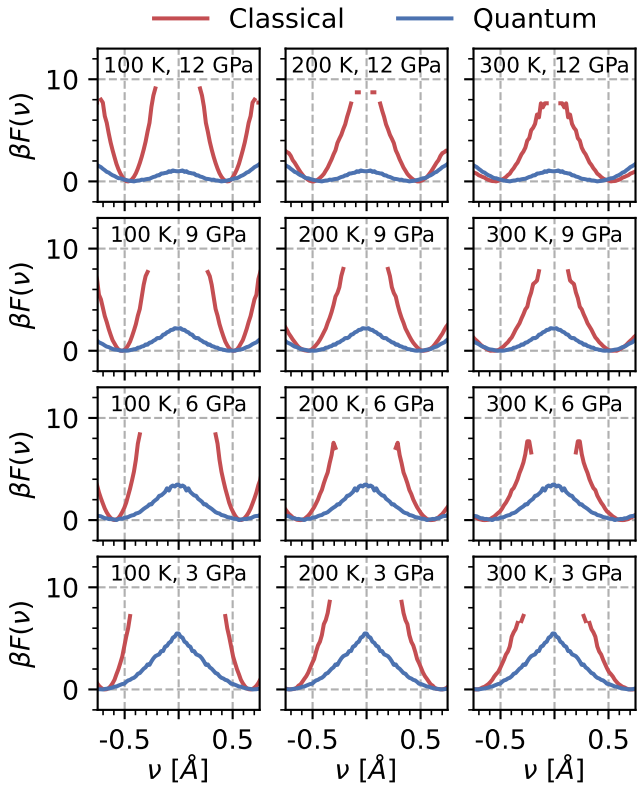

FIG. S5. **The temperature scaled free energy along the proton transfer coordinate for the flat-rhombic phase.** Each panel corresponds to a different thermodynamic state point. The classical and quantum free energy profiles are shown in red and blue, respectively.

Fig. S5 reports the classical and quantum proton transfer free energy profiles for the flat rhombic phase from 3-12 GPa and 100-300 K. On the timescales of our simulations, we do not observe proton transfer in any of our classical simulations of the flat-rhombic phase. Accordingly, we do not estimate the height of the classical free energy barrier. On the other hand, when NQEs are accounted for, we observe proton transfer at all of the selected state points, even down to 100 K and 3 GPa. As discussed in the main text, these proton transfer events in the flat-rhombic phase involve protons shuttling back and forth between adjacent water molecules, without any diffusive proton transport.

V. PROTON DIFFUSION IN HEXATIC WATER

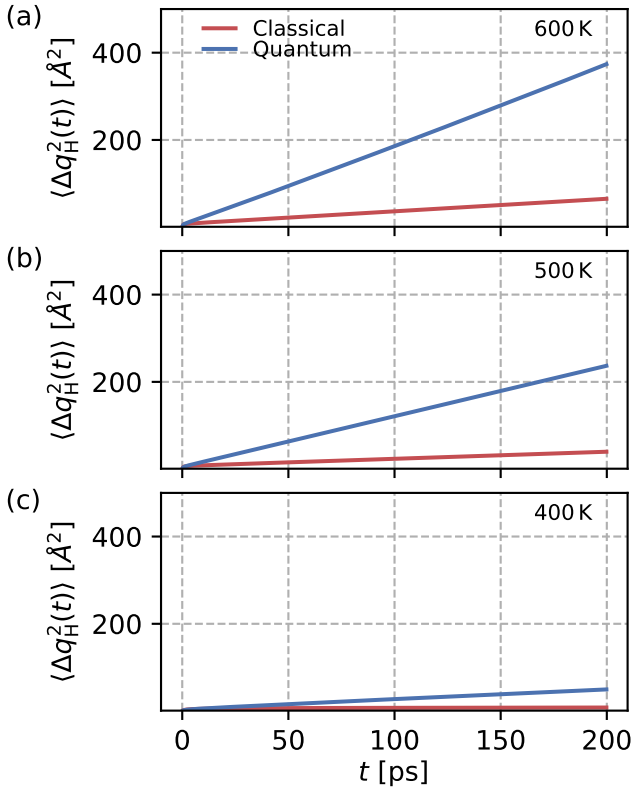

FIG. S6. **Mean squared displacement of protons in the hexatic phase at 12 GPa.** The classical and quantum mean squared displacements are shown in red and blue, respectively.

Fig. S6 reports the classical and quantum proton mean squared displacements for the hexatic phase at 12 GPa and 400-600 K. Over the same amount of time, NQEs lead to over an order of magnitude increase in the mean squared displacement for protons.

The Einstein-Helfand relation for ionic conductivity is given by $\sigma = \frac{\beta}{3V} \lim_{t\to\infty} \frac{\langle |\Delta\mu(t)|^2 \rangle}{2t}$, where V is the volume and μ is the total dipole moment, with partial charges assigned equal to the oxidation number of the atoms. Due to the β prefactor, any fixed statistical error in the mean squared displacement of the total dipole moment leads to a linearly increasing statistical error in the ionic conductivity. At low temperatures, this relation suffers from poor convergence, requiring very long trajectories. The β prefactor can result in an erroneous increase in ionic conductivity with decreasing temperature when the simulations are not long enough. This makes it difficult to compute the temperature dependence of ionic conductivity accurately, especially when O–H bonds remain intact. This can result in an erroneous increase in ionic conductivity with decreasing temperature. To avoid these statistical issues in identifying superionic behaviour, we focus on the fact that ionic conduction in superionic water is driven by O–H bond dissociation. A phase cannot be superionic without exhibiting dissociated O–H bonds. Hence, we plot the proton transfer barriers in Fig. S7 to check which simulations exhibit O–H dissociation. We estimate the ionic conductivity only for state points where O–H dissociation is observed. For these conditions, we achieve good statistical accuracy in estimating the ionic conductivity and can determine if the value exceeds the threshold of 0.1 S/cm.

Fig. S7 shows that our quantum simulations exhibit O–H dissociation at all state points in the 3-12 GPa and 400-600 K range. However, the classical simulations only exhibit O–H dissociation at the higher temperatures and lateral pressures. The ionic conductivities in Fig. S8 show a similar general trend. Our classical simulations only exceed the 0.1 S/cm threshold at 12 GPa and 500-600 K. However, the quantum simulations exhibit near-superionic proton transport in all simulations with a lateral pressure that is at least 6 GPa. Even the 3 GPa simulations show a non-trivial level of O–H dissociation, although they fail to meet the 0.1 S/cm cutoff for superionicity.

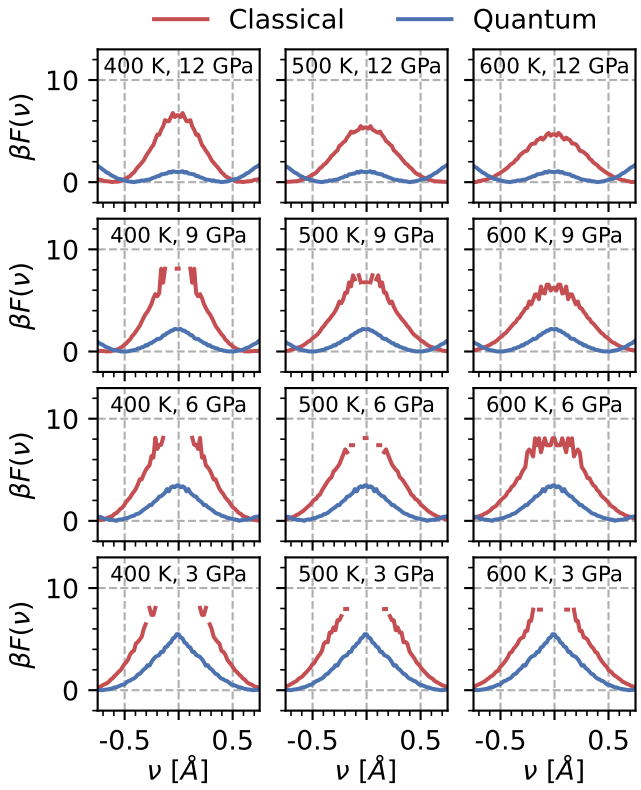

FIG. S7. **Analyses for identifying conditions which exhibit O–H dissociation.** The classical and quantum free energy profiles along the proton transfer coordinate ν are shown in red and blue, respectively. Each panel corresponds to a different thermodynamic state point.

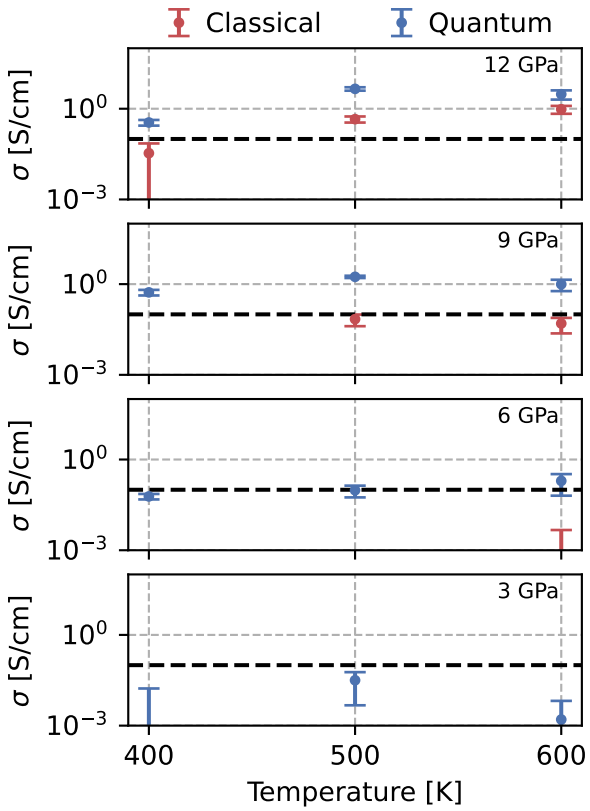

FIG. S8. **The ionic conductivity of the hexatic phase across a variety of conditions.** The classical and quantum ionic conductivities at 3-12 GPa for the temperatures that exhibit O–H dissociation on the timescale of our simulations. The horizontal dashed black line corresponds to the 0.1 S/cm cutoff that we use for superionic behaviour. For the data points where the error bars go off the plot, the error values are larger than the actual data values, meaning that the ionic conductivities are too close to 0 to provide a reliable estimate. Hence, the corresponding conditions clearly do not exhibit superionicity.

[1] J. Chen, A. Zen, J. G. Brandenburg, D. Alfè, and A. Michaelides, Evidence for stable square ice from quantum monte carlo, Physical Review B **94**, 220102 (2016).

[2] V. Kapil, C. Schran, A. Zen, J. Chen, C. J. Pickard, and A. Michaelides, The first-principles phase diagram of monolayer nanoconfined water, Nature **609**, 512 (2022).

[3] C. Schran, K. Brezina, and O. Marsalek, Committee neural network potentials control generalization errors and enable active learning, The Journal of Chemical Physics **153** (2020).

[4] P. Ravindra, X. R. Advincula, C. Schran, A. Michaelides, and V. Kapil, Quasi-one-dimensional hydrogen bonding in nanoconfined ice, Nature Communications **15**, 7301 (2024).

[5] G. Bussi, D. Donadio, and M. Parrinello, Canonical sampling through velocity rescaling, The Journal of chemical physics **126** (2007).

[6] M. Ceriotti and D. E. Manolopoulos, Efficient first-principles calculation of the quantum kinetic energy and momentum distribution of nuclei, Physical review letters **109**, 100604 (2012).

[7] F. Musil, I. Zaporozhets, F. Noé, C. Clementi, and V. Kapil, Quantum dynamics using path integral coarse-graining, The Journal of Chemical Physics **157** (2022).

[8] V. Kapil, D. P. Kovács, G. Csányi, and A. Michaelides, First-principles spectroscopy of aqueous interfaces using machine-learned electronic and quantum nuclear effects, Faraday Discussions **249**, 50 (2024).

[9] K.-D. Kreuer, Proton conductivity: materials and applications, Chemistry of materials **8**, 610 (1996).

[10] A. R. McCluskey, S. W. Coles, and B. J. Morgan, Accurate estimation of diffusion coefficients and their uncertainties from computer simulation (2024), arXiv:2305.18244 [cond-mat.stat-mech].

[11] A. R. McCluskey, A. G. Squires, J. Dunn, S. W. Coles, and B. J. Morgan, kinisi: Bayesian analysis of mass transport from molecular dynamics simulations, Journal of Open Source Software **9**, 5984 (2024).

[12] T. D. Kühne, M. Iannuzzi, M. Del Ben, V. V. Rybkin, P. Seewald, F. Stein, T. Laino, R. Z. Khaliullin, O. Schütt, F. Schiffmann, *et al.*, Cp2k: An electronic structure and molecular dynamics software package-quickstep: Efficient and accurate electronic structure calculations, The Journal of Chemical Physics **152** (2020).

[13] M. Kállay, P. R. Nagy, D. Mester, Z. Rolik, G. Samu, J. Csontos, J. Csóka, P. B. Szabó, L. Gyevi-Nagy, B. Hégely, *et al.*, The mrcc program system: Accurate quantum chemistry from water to proteins, The Journal of chemical physics **152** (2020).

[14] S. Goedecker, M. Teter, and J. Hutter, Separable dual-space Gaussian pseudopotentials, Physical Review B **54**, 1703 (1996).

[15] M. Guidon, J. Hutter, and J. VandeVondele, Auxiliary Density Matrix Methods for Hartree-Fock Exchange Calculations, Journal of Chemical Theory and Computation **6**, 2348 (2010).

[16] F. Neese and E. F. Valeev, Revisiting the atomic natural orbital approach for basis sets: robust systematic basis sets for explicitly correlated and conventional correlated ab initio methods?, Journal of chemical theory and computation **7**, 33 (2011).

[17] K. A. Peterson and T. H. Dunning Jr, Accurate correlation consistent basis sets for molecular core–valence correlation effects: The second row atoms al–ar, and the first row atoms b–ne revisited, The Journal of chemical physics **117**, 10548 (2002).

[18] M. Ceriotti, J. Cuny, M. Parrinello, and D. E. Manolopoulos, Nuclear quantum effects and hydrogen bond fluctuations in water, Proceedings of the National Academy of Sciences **110**, 15591 (2013).

[19] A. Hassanali, F. Giberti, J. Cuny, T. D. Kühne, and M. Parrinello, Proton transfer through the water gossamer, Proceedings of the National Academy of Sciences **110**, 13723 (2013).

[20] C. Richter, D. Hollas, C.-M. Saak, M. Förstel, T. Miteva, M. Mucke, O. Björneholm, N. Sisourat, P. Slavíček, and U. Hergenhahn, Competition between proton transfer and intermolecular coulombic decay in water, Nature Communications **9**, 4988 (2018).